

# 3D-Printable Bioactivated Nanocellulose–Alginate Hydrogels

Jenni Leppiniemi,<sup>†,‡</sup> Panu Lahtinen,<sup>§</sup> Antti Paaanen,<sup>§</sup> Riitta Mahlberg,<sup>§</sup> Sini Metsä-Kortelainen,<sup>§</sup> Tatu Pinomaa,<sup>§</sup> Heikki Pajari,<sup>§</sup> Inger Vikholm-Lundin,<sup>†,‡</sup> Pekka Pursula,<sup>§</sup> and Vesa P. Hytönen<sup>\*,†,‡</sup>

<sup>†</sup>Faculty of Medicine and Life Sciences and BioMediTech, University of Tampere, Lääkärintäti 1, 33520 Tampere, Finland

<sup>‡</sup>Fimlab Laboratories, Biokatu 4, 33520 Tampere, Finland

<sup>§</sup>VTT Technical Research Centre of Finland Ltd, P.O. Box 1000, 02044 VTT, Finland

## Supporting Information

**ABSTRACT:** We describe herein a nanocellulose–alginate hydrogel suitable for 3D printing. The composition of the hydrogel was optimized based on material characterization methods and 3D printing experiments, and its behavior during the printing process was studied using computational fluid dynamics simulations. The hydrogel was biofunctionalized by the covalent coupling of an enhanced avidin protein to the cellulose nanofibrils. Ionic cross-linking of the hydrogel using calcium ions improved the performance of the material. The resulting hydrogel is suitable for 3D printing, its mechanical properties indicate good tissue compatibility, and the hydrogel absorbs water in moist conditions, suggesting potential in applications such as wound dressings. The biofunctionalization potential was shown by attaching a biotinylated fluorescent protein and a biotinylated fluorescent small molecule via avidin and monitoring the material using confocal microscopy. The 3D-printable bioactivated nanocellulose–alginate hydrogel offers a platform for the development of biomedical devices, wearable sensors, and drug-releasing materials.

**KEYWORDS:** 3D printing, hydrogel, nanocellulose, alginate, avidin, wound healing



## 1. INTRODUCTION

Three-dimensional (3D) printing refers to the fabrication of objects layer by layer through the deposition of material using a printer head, nozzle, or some other printer technology.<sup>1</sup> Additive manufacturing or 3D printing technology is nowadays widely used in consumer and industrial applications, including motor vehicle manufacturing, aerospace manufacturing, and medical applications.<sup>2</sup> 3D printing enables lighter structures, better product performance, and lower production costs because separate molds and other manufacturing tools are not needed. In the medical field, the utilization of 3D printing has many advantages, especially through personalized products and mass customization. The medical sector uses 3D printing for the fabrication of models, surgical cutting or drill guides, and different kinds of implants.<sup>3–5</sup> In addition, 3D printing is utilized in tissue engineering and in wound-healing applications, in which it enables personalized shapes and tailored structures.<sup>6–9</sup>

Collapsing and shape fidelity are common challenges in 3D printing.<sup>6</sup> Collapsing is typical of biobased hydrogels, and it is usually due to a low dry-matter content. Shape fidelity, in turn, is related to the viscoelastic properties of the printing paste. Optimally, the paste should flow through the nozzle during the printing process and retain its shape after printing and curing. Rheology modifiers can be used to improve printability and to obtain shape fidelity after printing. One of the recently applied rheology modifiers is nanocellulose or, more specifically, cellulose nanofibrils (CNF), which are also potential carriers for functional components such as proteins. Another form of

nanocellulose, cellulose nanocrystals (CNC), has been used as a reinforcement in alginate-based composites and as a component in 3D-printable inks.<sup>10,11</sup> Some recent review articles cover alginate-based bioink formulations for biomedical applications, but only a few formulations that contain nanocellulose are described.<sup>12,13</sup>

3D-printable materials for biological applications have to fulfill requirements, such as being biocompatible and possessing low cytotoxicity. There are also application-specific requirements, such as in the case of wound healing, in which the printed structure has to keep its shape under wet conditions, support cell attachment and proliferation, and regulate the moisture level of the wound.

Hydrogels are three-dimensional polymer networks that have a high degree of flexibility and the capability to retain a large amount of water in their swollen state.<sup>14,15</sup> Hydrogels are composed of natural or synthetic polymers that are cross-linked either chemically by covalent bonds; physically by hydrogen bonding, hydrophobic interactions, and ionic complexation; or by a combination of both chemical and physical cross-linking.<sup>15,16</sup> Nontoxic hydrogels are often used in biomedical applications because they closely resemble biological tissues with regard to their high water content, morphology, and soft texture. Hydrogels also provide an ideal environment for wound healing, as it is widely accepted that maintaining a moist

**Received:** February 24, 2017

**Accepted:** June 9, 2017

**Published:** June 9, 2017

wound bed and skin hydration are needed for effective healing.<sup>17</sup>

The avidin protein is an interesting molecule for biofunctionalization due to its capability to bind to biotin with extremely high affinity ( $K_d \approx 6 \times 10^{-16}$  M) and specificity.<sup>18</sup> Biotin, also known as vitamin H, is a small molecule that contains a valeric acid tail that allows covalent fusion with many biomolecules without disturbing their biological function. Similarly, avidin can be covalently attached to biomaterials via its surface-exposed amino groups or by using a C-terminal cysteine introduced to the engineered avidin form.<sup>19</sup> The benefit of the avidin–biotin technology is that if the material can be functionalized with avidin, then in principle it can be activated with any biotinylated biomolecule, providing a generic platform for material functionalization. A vast amount of reagents related to avidin–biotin technology is commercially available. Because the avidin–biotin interaction is noncovalent, the biotinylated molecules may also be released from the matrix in situ. The release rate of biotinylated molecules could be tailored by using modified avidins with different affinities toward biotin.<sup>20,21</sup>

In this article, we describe a nanocellulose–alginate hydrogel suitable for 3D printing. The composition of the hydrogel was optimized based on material characterization methods and 3D printing experiments. In addition, the feasibility of computational fluid dynamics (CFD) simulations for predicting dependencies between the printing parameters and the hydrogel behavior were studied using separate models for the printer head and the deposition. The hydrogel was biofunctionalized by covalent coupling of an enhanced avidin protein to the cellulose nanofibrils. The 3D-printable bioactivated nanocellulose–alginate hydrogel offers a platform for the development of 3D bioprinting, wearable sensors, and drug-releasing materials for wound healing.

## 2. MATERIALS AND METHODS

**2.1. Materials.** TEMPO-oxidized cellulose nanofibrils (TCNF) were produced from never-dried bleached hardwood kraft pulp from Finland. 2,2,6,6-Tetramethylpiperidine-1-oxyl (TEMPO)-mediated oxidation was carried out as a chemical pretreatment according to the method applied by Saito et al.<sup>22</sup> The sample amount was 300 g, and the pulp was suspended in 30 L of purified water. TEMPO (0.1 mmol/g) and NaBr (1 mmol/g) were used to catalyze the oxidation reaction with NaClO (5 mmol/g). The pH was kept at 10 by adding 1 M NaOH during the reaction. When the pH level stabilized, the reaction was stopped by adding ethanol into the oxidized pulp suspension. Finally, the pH was adjusted to 7 by adding 1 M HCl. The oxidized pulp was washed with deionized water by filtration and stored in a fridge at +6 °C before fibrillation. The carboxyl content of the oxidized pulp was determined using conductometric titration according to the method described by Saito et al.<sup>22</sup>

The oxidized pulp was soaked at 1% solids and dispersed using a high-shear Ystral X50/10 Dispermix mixer for 10 min at 2000 rpm. The pulp suspension was then fed into Microfluidics' microfluidizer type M110-EH at a 1850 bar pressure. The suspension went twice through the chambers with diameters of 400 and 100  $\mu$ m. The final product formed a viscous and transparent hydrogel with a final dry material content of 1.06% and a charge value of 1.1 mmol/g dry pulp. The quality of the TCNF was characterized using rheological measurements and optical and atomic force microscopy (AFM) imaging. The rheological measurements are described later in this chapter.

Sodium alginate (E401) was provided by Cargill as a light-brown powder. The alginate Algogel 3541 had a medium mannuronic acid-to-guluronic acid ratio (~0.7–0.8). An aqueous solution of CaCl<sub>2</sub> (90 mM) was used as the cross-linking solution for the printed

structures. Glycerin (99.5%, AnalaR NORMAPUR) was purchased from VWR International. The phosphate-buffered saline (PBS) buffer was prepared at the University of Tampere with a salt composition that is given in the [Supporting Information](#).

N-(3-(Dimethylamino)propyl)-N'-ethylcarbodiimide hydrochloride (EDC) was obtained from Fluka (product ID 03450), and N-hydroxysuccinimide (NHS) was purchased from Pierce (product ID 24500). A charge-neutralized version of thermostable chimeric avidin (nChiAvd) was expressed in *Escherichia coli* and purified using affinity chromatography, as described earlier.<sup>23,24</sup> D-biotin was purchased from Fluka (product ID 14400). Prolong Diamond antifade mountant (Thermo Fisher Scientific) was used in the preparation of the samples for fluorescence microscopy. Fluorescent avidin ligand DY634-biotin from Dyomics was used to probe the activity of the biofunctionalized composite.

**2.2. Preparation of Hydrogels.** Several formulations of the printing pastes were prepared from pure TCNF and a mixture of TCNF, alginate, and glycerin. The aim of the preliminary trials was to formulate pastes that have suitable viscoelastic properties, so that they flow through the nozzle and retain their structure after being deposited. In addition, the aim was to increase the volume and the share of nonvolatile components so that excessive shrinkage could be minimized and the specimen would retain their shape after being cured. For this reason, part of the water was replaced with glycerin. After the preliminary trials, four pastes with different compositions were selected for further evaluation (Table 1).

**Table 1. Printing Paste Formulations Chosen for Further Evaluation**

sample ID	alginate/TCNF (w/w)	water (% w/v)	glycerin (% w/v)
TCNF	0/100	99	0
AT	66/33	96	0
ATG30	85/15	65	30
ATG50	90/10	45	50

TCNF was used as a reference gel in with dry matter content of 1.06%. When glycerin was not included, the alginate powder was mixed directly with TCNF. The powder was added gradually into the hydrogel while the paste was intensively mixed with a spoon for 2 min. When glycerin was used, the alginate powder was first mixed with glycerin until a smooth low-viscosity fluid was formed. Next, TCNF was added into the mixture and blended rapidly. In less than 30 s, the mixture became an exceptionally viscous paste. All of the pastes were stored in a fridge at 6 °C before printing.

**2.3. Preparation of Samples for Microscopy.** Optical microscopy and AFM imaging were used to study the assembly of the hydrogels. Samples for the optical microscopy were prepared according to the method described by Kangas et al.<sup>25</sup> Toluidine Blue (0.1%) was used as the marker color instead of a Congo red solution. Diluted samples were also prepared for AFM imaging. Suspensions were cast onto silicon dioxide sheets by using a simple drop-casting method. All samples were first diluted 1:100 in Milli-Q water. After dilution, the solutions were gently shaken (manually) followed by addition of a couple of droplets on the SiO<sub>2</sub> sheets. Water was evaporated from the droplet by keeping the samples in an oven at 80 °C for 10 min. Nanoscale characterization of the finest fraction of the prepared TCNF and the ATG50 mixture was performed with AFM (Anasys Instruments AFM+, Santa Barbara, CA). The AFM characterization was carried out with MicroMash AFM cantilevers with a tip radius of 8 nm. At least three spots on a specimen were investigated.

**2.4. Covalent Conjugation of Avidin to TCNF using NHS and EDC Chemistry.** To produce a hydrogel with biofunctionalization capability, avidin was covalently attached to CNFs. nChiAvd, an ultrastable avidin form with neutral isoelectric point presented earlier was utilized here.<sup>23</sup> Lyophilized nChiAvd was dissolved in distilled water at a concentration of 1 mg/mL. TCNF (1.06%) was sonicated (Sonics & Materials VC 505 Sonicator) using a 5 mm probe with a

25% amplitude for 2 min on an ice bath to homogenize the material and detach nanocellulose fibrils and aggregates from each other. Sonicated TCNF was mixed with an aqueous suspension of EDC and NHS to a concentration of 50 and 125 mM, respectively, and incubated at room temperature [RT],  $21 \pm 1$  °C) for 15 min. 2-Mercaptoethanol was added to the reaction with a final concentration of 20 mM to quench unreacted EDC. nChiAvd (1 mg/mL) was added to activated TCNF for covalent conjugation. As a control sample, TCNF was used without EDC or NHS activation. The control sample was diluted with distilled water to the same extent that the activated TCNF before addition of nChiAvd. Reactions were mixed well and incubated on a rolling shaker for 2 h at RT. Finally, the reaction was quenched by adding Tris-HCl (pH 8) to a final concentration of 20 mM. To remove the excess of reagents, the samples were dialyzed against distilled water using a 1000 kDa dialyzing tubing (Spectra/Por Dialysis Membrane, Spectrum Laboratories, Inc., Rancho Dominguez, CA).

**2.5. SDS-PAGE.** Sodium dodecyl sulfate polyacrylamide gel electrophoresis (SDS-PAGE) was used for analyzing the covalent conjugation of nChiAvd to TCNF. Samples were analyzed both in the absence and in the presence of D-biotin, as biotin is known to stabilize the nChiAvd tetramer. Samples were incubated with a 10-fold molar excess of D-biotin (Fluka Chemie GmbH, Buchs, Switzerland) for 1 h at RT. Samples without biotin were diluted with distilled water to the same extent. A total of four parts of the sample were diluted with one part of a 5× SDS-PAGE sample-loading buffer containing  $\beta$ -mercaptoethanol and heated either to 50 or 100 °C for 20 min. Then, the samples were loaded to a Mini Protean TGX stain-free precast gel (Bio-Rad Laboratories, Hercules, CA) in SDS-PAGE running buffer and run at 300 V for 15 min followed by detection with a UV-induced reaction by a ChemiDoc MP imaging system (Bio-Rad Laboratories) with Image Lab software.

**2.6. 3D Printing.** VTT's microdispensing environment, based on nScrip technology, was used in the 3D printing of the hydrogels containing different proportions of TCNF, alginate, glycerin, and nChiAvd. A quick evaluation of their printability was performed with a 0.5 mm diameter nozzle attached onto a 10 mL syringe. When the material performance was regarded as appropriate for printing, the trials continued with a printing device. The 3D structures were printed on plastic substrate in a layer-by-layer approach using a CAD controlled xyz motion-control system that guides the tip position. A simplified pump system based on air pressure controlled dispensing of the hydrogels through a tip was utilized.

The hydrogels were inserted into 3 mL syringes, which were then put in a speed mixer (SpeedMixer DAC 150 SP) for 2–8 min to remove air bubbles and to ensure sample uniformity. For the development of the hydrogel formulations, the printability of the materials and the stability of the 3D-printed structures were studied in a qualitative manner. The target was to create a good flow of the hydrogels through the printing tip by adjusting several printing parameters such as air pressure; speed, height of the tip from the substrate; distance between the layers; and selection of the size, shape, and material of the tip.

A summary of the tests and 3D structures is given in Table 2. Plastic tips of 0.41 mm diameter were used to print the structures containing glycerin, while the other structures were printed using polytetrafluoroethylene-coated steel tips of 0.15 mm diameter or plastic tips of 0.20 mm diameter. A printing speed of 2 mm/s was used in all cases.

**Table 2. Structures 3D-Printed for Detailed Characterization**

test	3D structure	number of layers	parallel samples
conditioning tests	14 × 14 mm <sup>2</sup> grid with 2 mm squares	20	4
buffer tests	34 × 34 mm <sup>2</sup> grid with 2.8 mm diamonds	6	2
functionalization tests	14 × 14 mm <sup>2</sup> grid with 2 mm squares	2	2

Certain specimens were cross-linked in a bath of 90 mM CaCl<sub>2</sub> for 3–10 min according to Markstedt et al.<sup>6</sup> and then rinsed with Milli-Q water. Samples without glycerin were frozen and furthermore freeze-dried immediately after the 3D printing.

A pair of 3D printing experiments were used to validate the CFD simulations. These include determining (i) the dependency between operating pressure and mass flux within the printer head and (ii) the dependency between line resolution and printing speed at a constant operating pressure. In the mass flux experiments, the printing paste was dispensed on a substrate for 20 s at operating pressures ranging from 1 to 30 PSI. A total of three parallel samples were printed, and their masses were weighed. Cylindrical steel tips of 0.2 mm and 0.51 mm were used for printing the TCNF paste, and a conical plastic tip of 0.41 mm was used for the ATG50 paste. In the line-resolution experiments, three parallel lines of 10 cm were printed on a graph substrate at operating pressures ranging from 1 to 10 PSI. The lines were then photographed (TCNF) or measured with a 3D optical profilometer (ATG50) for the determination of their width and profile. A cylindrical steel tip of 0.2 mm was used for printing the TCNF paste, and a conical plastic tip of 0.41 mm was used for the ATG50 paste.

**2.7. Buffer Tests.** The printed grids (Table 2) were soaked in PBS buffer to evaluate their structural stability and the effect of cross-linking in a wet condition. Structural changes were followed by taking photographs of the samples after they had soaked in the buffer for a predefined time. One of the printed specimens was cross-linked in a bath of 90 mM CaCl<sub>2</sub> for 3 min before the test, while the other printed specimen was not cross-linked.

**2.8. Conditioning Tests.** The moisture uptake and swelling behavior of the 3D-printed specimens (Table 2 and Figure 1) when stored at 90% relative humidity (RH) were evaluated by measuring their mass and dimensional changes. The 3D-printed structures of the ATG50 hydrogel, with and without CaCl<sub>2</sub> cross-linking, were placed in a humidity room of 50% ( $23 \pm 2$  °C) and stored under these conditions until the equilibrium weight was reached. 3D structures made from the TCNF hydrogel were used as reference specimens. The printed reference structures were freeze-dried to prevent the structures from collapsing. After drying, the TCNF reference specimens were conditioned to 50% RH equilibrium moisture content. Hereafter the specimens were moved to 95% RH, and mass and volume measurements were carried out three times a day at the minimum. Dimensional measurements were carried out by means of a digital vernier gauge with 10  $\mu$ m accuracy. Moisture absorption and volumetric swelling calculations were based on the relative change in weight and volume as a function of conditioning time.

**2.9. Compression Measurements.** Compression measurements were performed with a TAXT Plus Texture Analyzer and Exponent software at RT. Cast discs and printed square grids were conditioned before the tests at 50% RH and at 23 °C. Freeze-dried grids were prepared from both the TCNF and AGT50 samples. The discs had a diameter of 25 mm, and the height varied between 4–7 mm. The length of the grid side was between 17–19 mm, and the height was 5 mm. The samples were compressed until 30–70% compressive strain was achieved after reaching a trigger load of 1 g. Some sample discs had a convex surface and thus, they were compressed until 70% strain. Also, due to the uneven shape of the test specimen, the compression force at 30% strain was plotted as a function of the sample density.

**2.10. Rheometry.** Rotational rheometer experiments were used to study the rheological behavior of the printing pastes. The measurements were carried out using an Anton Paar MCR 301 rheometer with (i) vane spindle and cylindrical cup, (ii) concentric cylinder (CC), and (iii) plate–plate (PP) geometries. The CC-measuring head (CC27) had a cup radius of 14.46 mm and a measuring cylinder radius of 13.33 mm. The same cup was used with the vane spindle (ST22–4 V-40), which had four (11 mm) vertical vanes. The PP-measuring plate (PP50) had a radius of 25 mm, and the used measuring gap was 1 mm. All measurements were performed at 23 °C.

Dependence of the shear viscosity on shear rate was measured for both steady-state and transient conditions. In the steady-state



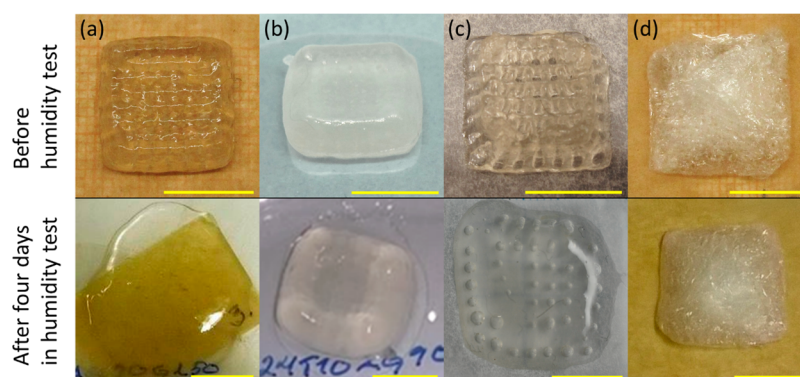


**Figure 1.** Printed hydrogel structures before the humidity tests (upper row) and after 4 days in the humidity chamber (lower row): (a) ATG50 non-cross-linked, (b) ATG50 cross-linked, (c) ATG50 freeze-dried, and (d) TCNF reference. The yellow scale bars indicate 10 mm.

experiments, each considered shear rate was sampled for at least 200 s, such that the viscosity would have converged. The steady-state viscosity was obtained by averaging the last 20 measured values (i.e., 20 s at 1 Hz sampling frequency). In the transient experiments, the sample was first pre-sheared at a constant rate until the steady-state viscosity was reached. The shear rate was then suddenly increased or decreased by several orders of magnitude, and the time evolution of the viscosity was followed. The maximum shear rate used with the vane spindle and cylindrical cup geometry was  $316 \text{ s}^{-1}$ . With the CC and PP geometries, the range could be extended to  $3160 \text{ s}^{-1}$ . The minimum shear rate was  $10^{-4} \text{ s}^{-1}$  for all the geometries.

The hydrogels' yield flow behavior was also determined by rheometry. The measurements were done using the stress ramp method, in which the stress-controlled rheometer applies a constantly increasing shear stress while measuring the induced strain. The yield stress is found at the viscosity maximum. Stress ramp rates between 0.2 and  $1.7 \text{ Pa} \cdot \text{s}^{-1}$  were considered in the yield stress measurements.

**2.11. CFD Simulations.** CFD simulations were used to study the flow conditions within the printer heads and in the deposition. Printer-head models were used to determine the dependence between hydrogel mass flux, printer-head geometry, and operating pressure as well as the associated shear stress levels. Deposition models, in turn, were used to relate the profile of the printed line with operating pressure and printing speed.

Both printer-head geometries (Figure 2) were described by an axisymmetric mesh of roughly  $10^4$  volume elements. The stainless steel

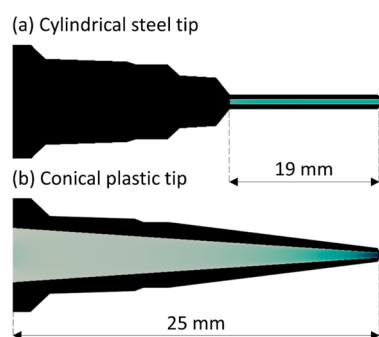


**Figure 2.** Printer head geometries: (a) the cylindrical steel tip and (b) the conical plastic tip. The black regions indicate the outline of the printer head, while the green regions indicate the interior volume considered in the CFD models.

tip was represented by a segment of the straight cylindrical geometry and the plastic tip by the full conical geometry. The hydrogel inlet was described by a uniform velocity boundary condition, and the interior surface of the tip was described by a no-slip boundary condition.

The deposition geometry was described by a hexahedral mesh of roughly  $10^6$  volume elements. The following boundary conditions

were used: (i) the printing tip was reduced to a circular hydrogel inlet at the top boundary, with a uniform velocity boundary condition; (ii) the substrate was described as a moving wall with a velocity opposite to that of the printer head; (iii) the frontal open-air boundary was described as an air inlet with a velocity opposite to that of the printer head; (iv) the back open-air boundary was described as an outlet; and (v) the top and side open-air boundaries were described as far-field boundaries. The substrate was set to reproduce a fixed contact angle with the hydrogel, as determined by goniometer experiments. The hydrogel–air surface tension was set to a value slightly lower than that for pure water and air. The volume of fluid (VOF) method was used to describe the interaction of the hydrogel with the surrounding air, which was modeled as a Newtonian fluid. Both fluids share the same set of momentum equations. The turbulent flow conditions in air were taken into account with a standard K- $\epsilon$  model.

The shear-thinning behavior of the hydrogel was described using the power-law fluid model:

$$\eta = K\dot{\gamma}^{n-1} \quad (1)$$

where  $\eta$  is the dynamic viscosity,  $\dot{\gamma}$  is the shear rate,  $K$  is the flow consistency index, and  $n$  is the flow behavior index. Moreover, the time-dependence of the shear-thinning behavior was considered using a kinetic thixotropy model, which describes the breakdown and build-up rate of the gel network.<sup>26</sup> The considerations related to thixotropy are given in Supporting Information. The open-source software OpenFOAM<sup>27</sup> was used for the CFD simulations.

**2.12. Bioactivity Analysis of 3D-Printed Constructs.** 3D-printed samples containing covalently bound avidin (ATG50–nChiAvid) were incubated with 100 nM DY634-biotin (Dyomics) in water overnight at RT, and then the samples were washed by flushing 10 times with distilled water to remove the unbound DY634-biotin. Similarly, 3D-printed samples (ATG50–nChiAvid) were incubated with 0.5, 1, or 2  $\mu\text{M}$  biotinylated enhanced green fluorescent protein (biotin–EGFP) in PBS containing 0.9 mM  $\text{CaCl}_2$  overnight at RT. The production and purification of biotin–EGFP has been described previously.<sup>19</sup> The samples were washed by flushing 10 times with PBS to remove the unbound biotin–EGFP. Finally, samples were washed with distilled water to remove the salts from the sample. For all experiments, control samples were preincubated with 1  $\mu\text{M}$  D-biotin for 1 h before addition of fluorescent biotin conjugates. Samples were placed on microscope slides, the excess of water was removed, and the samples were mounted in Prolong Diamond antifade mountant (Thermo Fisher Scientific). Then samples were imaged by confocal microscope (Zeiss LSM 780 LSCM) to determine the fluorescence distribution within the samples.

## 3. RESULTS

**3.1. Characterization of the Printing Pastes.** The visual appearance of the pure TCNF and ATG50 hydrogels is shown in Figure 3. TCNF was a transparent and viscous hydrogel, which changed to a slightly yellowish tone after the addition of



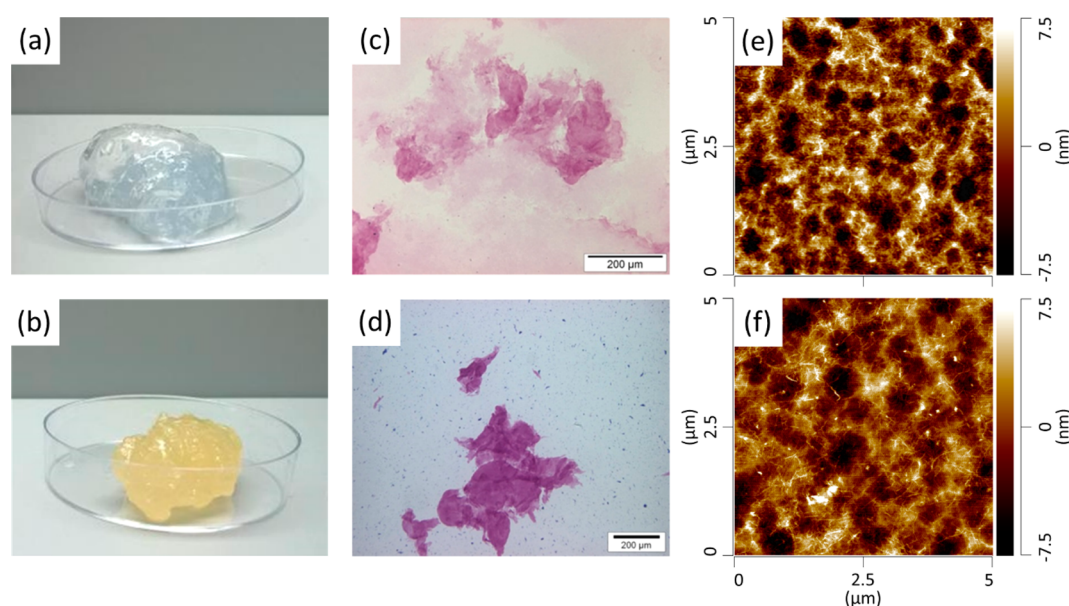


**Figure 3.** Photographs of the printing pastes (left column), optical microscopy images (middle column) and AFM images (right column) of TCNF (panels a, c, and e) and ATG50 (panels b, d, and f). The image z-range in the AFM images is 15 nm.

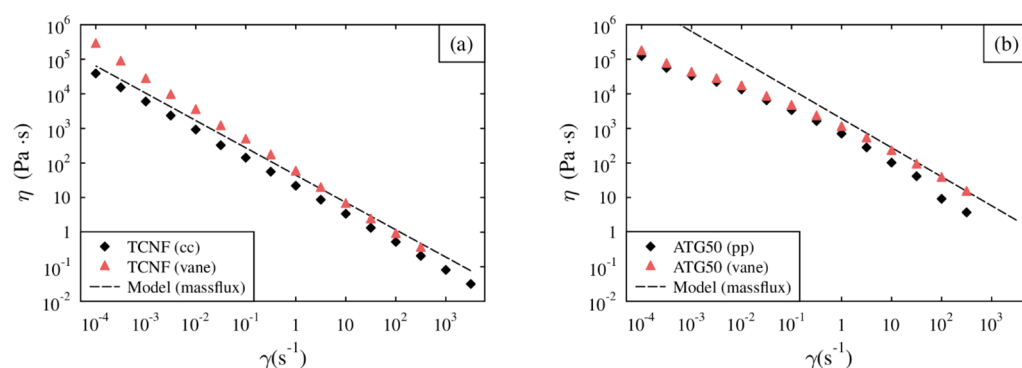


**Figure 4.** Steady-state viscosity as a function of shear rate in the rheometer experiments (a) for the TCNF hydrogel and (b) for the ATG50 hydrogel. In both plots, the dashed line corresponds to the power-law fluid model that reproduces the correct mass flux-operating pressure relationship in the CFD simulations.

alginate. Also, the increase in total dry-matter content could be seen in the rheological characteristic, which will be discussed later in this chapter. ATG50 was clearly more viscous and sticky. Optical microscopy and AFM images of TCNF and ATG50 are shown alongside the photographs in Figure 3. The optical images show only minor variation in the sample appearance. The samples did not contain any large fiber fragments or unfibrillated material, but some micrometer-sized agglomerates could be observed in ATG50. The colored patches in the optical microscopy images are gel structures that contain very fine fibrils. These structures absorb the marker color used in the sample preparation. The AFM images show fibrils with a width of approximately 3–10 nm. The presence of alginate could be seen in the agglomerates as a nonfibrous material.

**3.2. Rheometry.** The hydrogels were studied using rheometry to evaluate their flow properties and to enable further studies using CFD simulations. Rotational rheometer experiments were carried out for the TCNF and ATG50 hydrogels. Figure 4 shows the observed dependence of steady-state viscosity on shear rate for both materials. For TCNF, the whole range of shear rates from 10<sup>-4</sup> to 3160 s<sup>-1</sup>

could be measured. The hydrogel displays clear power-law behavior, as evidenced by the linear relationship in the logarithmic plot, and there are no signs of leveling at either high or low shear rates. Thus, the asymptotic values cannot be acquired with the used measurement technique. For ATG50, measurements at high shear rates proved problematic: the hydrogel was clearly viscoelastic, and it tended to brim over the measuring cup due to the Weissenberg effect. Due to this, measurements using the CC geometry were rejected, and the maximum shear rate was restricted to 316 s<sup>-1</sup>. ATG50 displays approximate power-law behavior within the measured shear rate range and had an observable deviation from linearity in the logarithmic plot. In terms of the power-law fluid model, the deviation corresponds to a flow-behavior index that is a decreasing function of shear rate. In other words, the shear-thinning character of the hydrogel becomes more pronounced toward higher shear rates. Again, there are no signs of leveling at either high or low shear rates, and it seems probable that the asymptotic values cannot be acquired with the used measurement technique.

The steady-state viscosity data was fitted against the power-law fluid model (eq 1) to obtain the corresponding flow

consistency and flow behavior indices. The parameter values are given in Table 3. Moreover, the transient shear rate

**Table 3. Material Parameters for the Power-Law Fluid Model**

material	experiment <sup>a</sup>	$k$ (Pa·s <sup><math>n</math></sup> )	$n$
TCNF	rheometry, CC	22.0	0.19
TCNF	rheometry, vane	55.6	0.10
TCNF	printing, mass flux	44.0	0.21
ATG50	rheometry, PP	420	0.32
ATG50	rheometry, vane	787	0.39
ATG50	printing, mass flux	1920	0.16

<sup>a</sup>Experiment on which the model is based.

experiments were used to construct a kinetic thixotropy model that describes the time-dependency of the shear-thinning behavior (see the Supporting Information).

Both TCNF and ATG50 exhibit yield-flow behavior. For TCNF, the measured yield stress is approximately 45 Pa, and for ATG50, it is approximately 300 Pa. After the gel network is broken, both hydrogels flow even if the applied shear stress is lower than the yield stress. This was observed when measuring the steady-state viscosities for gradually decreasing shear rates. For example, for TCNF, the shear stress at the lowest measured shear rate ( $10^{-4}$  s<sup>-1</sup>) is 24 Pa, which is well below the yield stress. The hydrogels would regain their gel strength when allowed to stand undisturbed for a longer time.

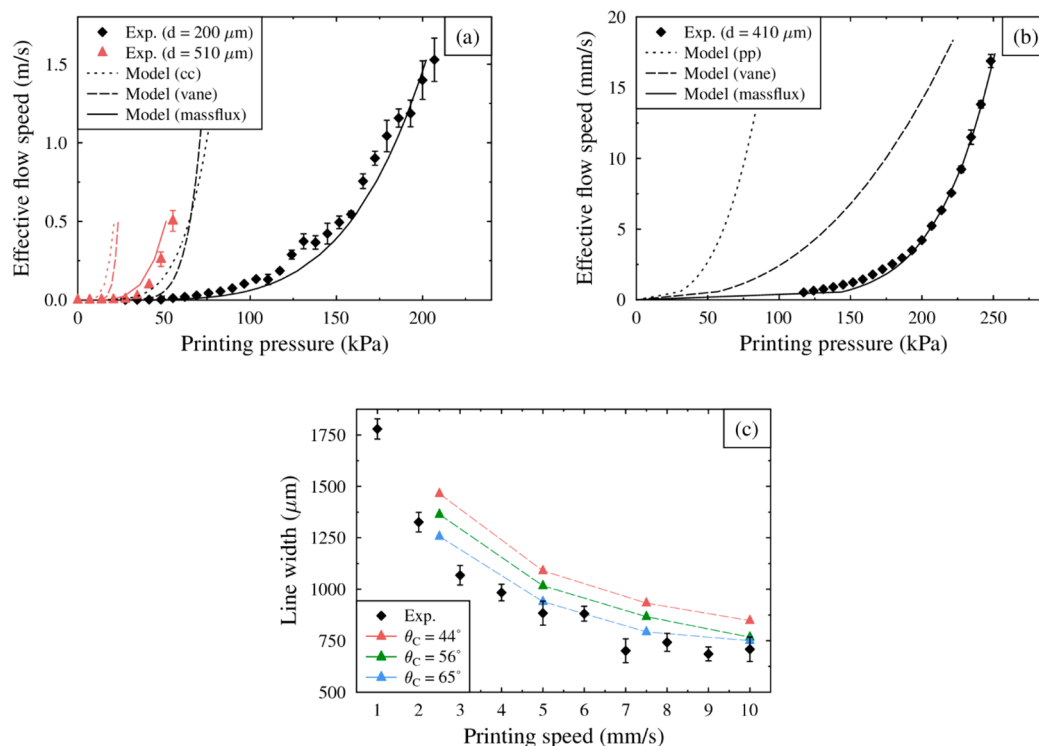
**3.3. CFD Simulations.** CFD simulations were used for predicting the printability of the hydrogels and printer-head models were used to predict the dependence between hydrogel mass flux, printer-head geometry, and operating pressure. Figure 5a shows a comparison between the CFD predictions

and experimental results for the TCNF hydrogel printed through 0.20 and 0.51 mm cylindrical steel tips, and Figure 5b shows a similar comparison for the ATG50 hydrogel printed through a 0.41 mm conical plastic tip.

The printer-head models severely overestimate the hydrogel mass flux at practical operating pressures when the power-law fluid model is based on the rheometer experiments. This suggests that the hydrogels' shear-thinning behavior begins to deviate from the power-law fluid model at shear rates above those used in the experiments. The deviation would correspond to a flow behavior index that is an increasing function of shear rate (such behavior has indeed been observed for CNF suspensions).<sup>28</sup> It is possible to test this proposition by fitting the power-law fluid model against the printing results themselves and by comparing the obtained model against the measured steady-state viscosities (as shown in Figure 4).



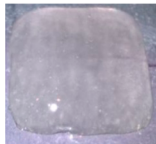
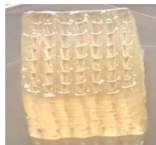
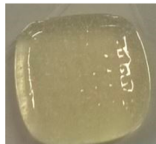
For the TCNF hydrogel, the model is roughly in agreement with the dynamic viscosity measurements. The predictions lie, for the most part, between the values obtained using the different measuring geometries. The flow behavior index is somewhat higher (see Table 3), as expected. This leads us to conclude that the pressure losses within the printing tip are indeed dictated by the hydrogel's viscosity at high shear rates, at least above  $10$  s<sup>-1</sup>. Shear rates predicted by the printer head model reach values as high as  $10^5$  s<sup>-1</sup>, which further supports the conclusion.

For the ATG50 hydrogel, the model clearly overestimates the dynamic viscosity at low shear rates but then converges with the values measured using the vane spindle and cylindrical cup geometry at shear rates above  $10$  s<sup>-1</sup>. Again, the pressure losses within the printing tip seem to be dictated by the hydrogel's dynamic viscosity at high shear rates, at least above  $10$  s<sup>-1</sup>. Shear rates predicted by the printer-head model reach values as



**Figure 5.** 3D printing experiments and CFD simulations. Effective flow speed within the printer head as a function of operating pressure (a) for the TCNF hydrogel and (b) for the ATG50 hydrogel. Line resolution as a function of printing speed (c) for the TCNF hydrogel.

Table 4. Paste Formulations and 3D Printing Parameters

Paste	Mixing time (min)	Air pressure (psi)	Post treatment	Printed structure
TCNF	2	11	Freezer / freeze-drying	
AT	2	23	Freezer / freeze-drying	
ATG30	4	65	Freezer / freeze-drying	
ATG50	8	22	Storage at room temperature	
ATG50-nChiAvd	4	20	Cross-linking 10 min, storage at room temperature	

high as  $10^3 \text{ s}^{-1}$ , which, once again, supports the conclusion that the pressure losses within the printing tip are dictated by the hydrogel's viscosity at high shear rates.

To summarize, when the power-law fluid model is fitted against conventional rheometer experiments, the hydrogel viscosity (and, thereby, the flow characteristics) within the printing tip is not predicted reliably. This is because the rheometer experiments measure lower shear rates than those that occur within the printing tip and because the shear thinning behavior seems to plateau toward the high shear rates.

Deposition models were used to predict the dependence between line resolution and printing speed at constant operating pressure. Figure 5c shows a comparison between the CFD predictions and experimental results for the TCNF hydrogel printed through a 0.20 mm cylindrical steel tip at 74.5 kPa operating pressure. The predictions fall within 50–100  $\mu\text{m}$  of the measured values, depending on the contact-angle boundary condition. This corresponds to a 6–13% over-prediction for the line resolution. Much of the uncertainty comes from the goniometer experiments, in which repeated measurements of the steady-state contact angle yielded values ranging from  $42^\circ$  to  $72^\circ$ . The deposition simulations proved not to be sensitive to the high shear rate values of dynamic viscosity.

The deposition simulations of the ATG50 hydrogel proved problematic for the VOF method. ATG50 is significantly more viscous than TCNF, and this, it turned out, led to numerical instabilities. In particular, the large viscosity difference at the hydrogel–air interface created large viscous stresses, and

thereby artificial currents, that are sensitive to the mesh resolution and the used numerical schemes. This implies that the single-fluid VOF-based model might not be appropriate for high-viscosity fluids like ATG50. For this reason, the results of the ATG50 deposition simulations are not presented. A more-robust approach would be to treat the hydrogel and air with separate set of momentum equations. This is usually done by tracking the interface explicitly with an arbitrary Lagrangian–Eulerian (ALE) finite element method.

**3.4. 3D Printing.** 3D-printability would enable the use of the materials in applications requiring personalized wound dressing shapes, for example. Therefore, printability and stability after the 3D printing of numerous different hydrogel formulations were studied, and the materials were tuned through a trial-and-error method. A total of five paste formulations were chosen for the further tests. The parameters and variables qualitatively selected for the 3D printing as well as pictures of the samples taken right after the 3D printing are shown in Table 4.

The hydrogels without glycerin were not stable at room temperature, and for that reason, the materials were freeze-dried before the next steps. The sample pictures show that TCNF and ATG50 were the best materials for 3D printing. The grid structure and different layers can be distinguished clearly. However, TCNF structures collapsed mainly due to evaporation of water without immediate freezing of the sample, while ATG50 proved to be very stable at room temperature. Freeze-dried TCNF structures were also very fragile and quite hard compared with the ATG50 structures, which were elastic.



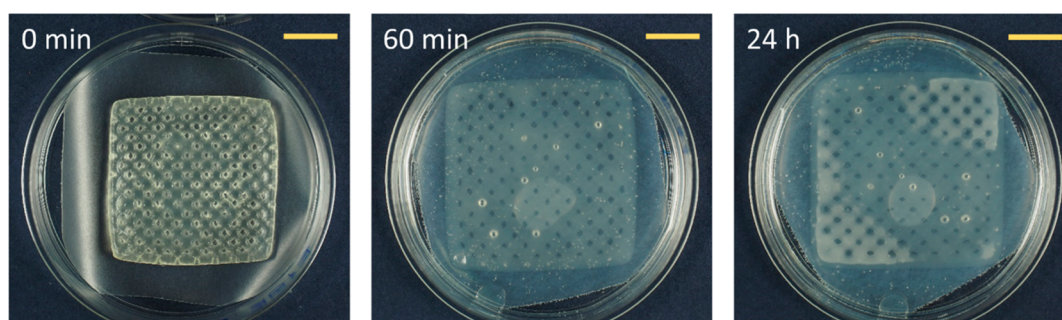


**Figure 6.** Cross-linked ATG50 grid in the PBS buffer. The yellow scale bars indicate 10 mm.

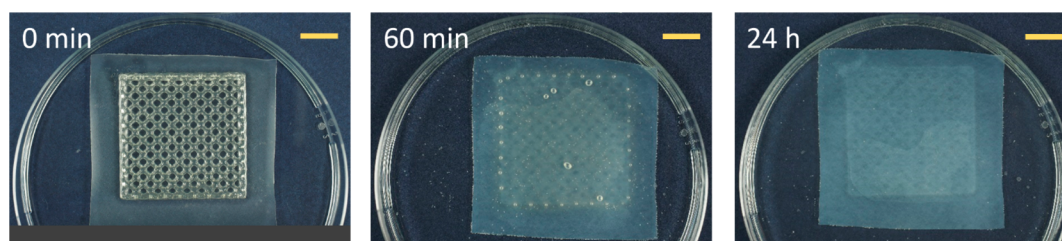


**Figure 7.** Non-cross-linked ATG50 grid in the PBS buffer. The yellow scale bars indicate 10 mm.

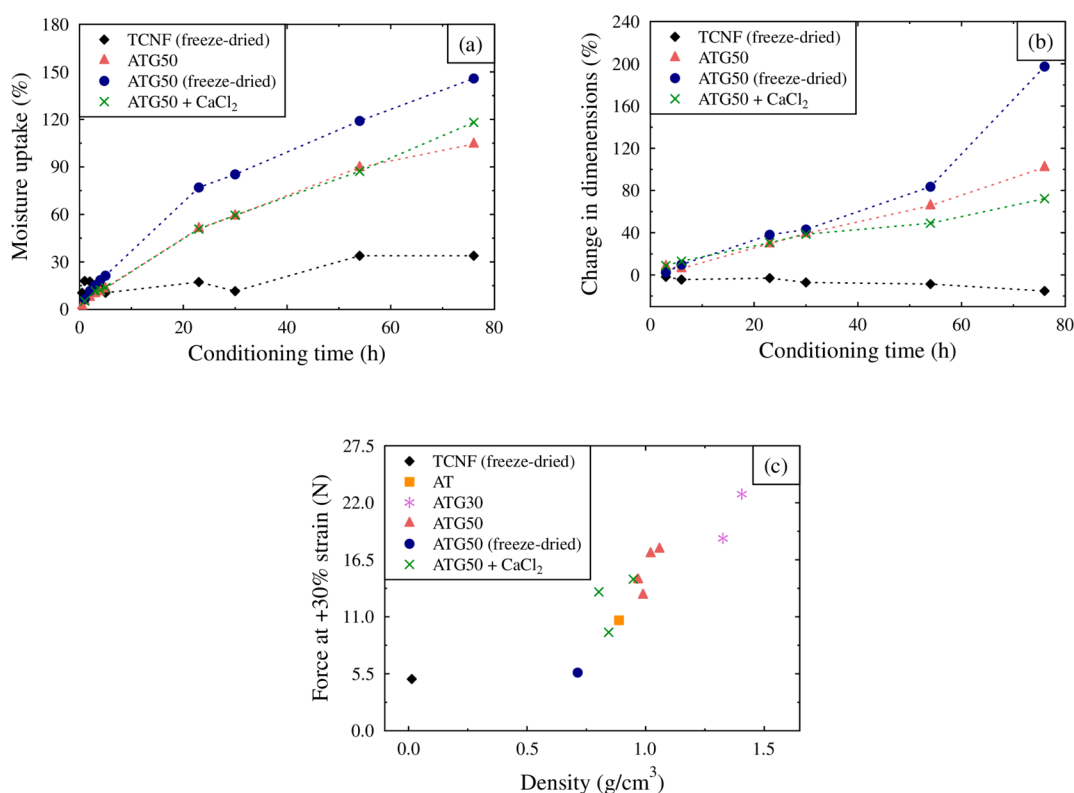


**Figure 8.** (a) Moisture absorption rates and (b) dimensional changes of the 3D-printed ATG50 structures and the reference sample (TCNF). (c) Compression test for samples of different material compositions before cross-linking.

**3.5. Buffer Testing.** Our ultimate goal is to develop biocompatible hydrogels. Therefore, the behavior of the hydrogel in the physiological environment is important. We simulated the biomedical use by exposing the printed hydrogels to a PBS buffer. The buffer test results are presented in Figures 6 and 7. The dimensional stability of the printed AGT50 grids, one cross-linked and one without cross-linking, were evaluated after 10 min, 60 min and 24 h when soaked in the PBS buffer.

The widths of the empty spaces and printed lines of the grids were approximately 1.6 and 1.1 mm, respectively, before the buffer test. The cross-linking almost doubled the line widths of the grids (1.9 mm), and the empty spaces shrank to 0.6–1.0 mm. In addition, the cross-linking caused slight dimensional shrinking of the outer edges of the grids from 34 to 32 mm. These changes resulted in a less-defined grid

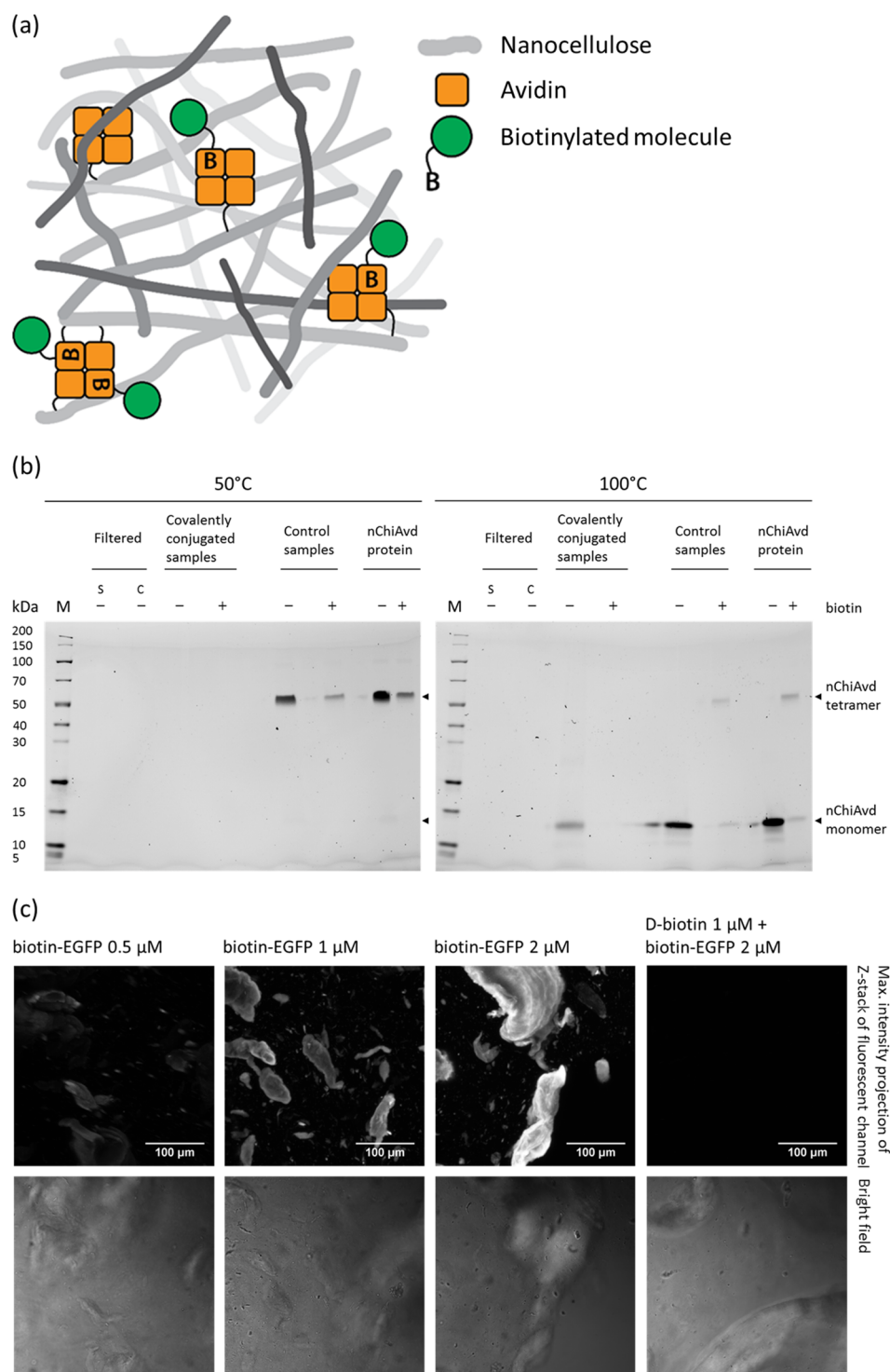


**Figure 9.** Biofunctionalization of nanocellulose by avidin. (a) A schematic showing the bioactivation principle in which avidin is covalently bound to nanocellulose. Avidin can be used to immobilize biotinylated target molecule. (b) SDS-PAGE analysis of covalent conjugation of nChiAvid by NHS and EDC chemistry to TCNF. M is the molecular weight marker. Covalently conjugated samples, control samples in which nChiAvid was mixed with TCNF without NHS and EDC activation, and nChiAvid protein samples were analyzed in the absence (–) and in the presence (+) of free D-biotin. The covalently conjugated sample (S) and control sample (C) was also filtered through a 0.2  $\mu\text{m}$  filter, and the filtrates were analyzed. Samples were heated to either 50 or 100  $^{\circ}\text{C}$  for 20 min and analyzed by electrophoresis. (c) Confocal microscope image analysis of 3D-printed samples containing covalently bound avidin (ATG50-nChiAvid) using fluorescent biotin–EGFP. The fluorescence of samples incubated with biotin–EGFP at increasing concentration (images from the left to the right, middle section: 0.5, 1, and 2  $\mu\text{M}$ ) are shown. As a control (image on the right), the sample was preincubated with free D-biotin (1  $\mu\text{M}$ ) before the addition of fluorescent biotin–EGFP (2  $\mu\text{M}$ ). Maximum intensity projections of Z-stack (upper row) and bright-field images of the same imaging spots (lower row) are shown, indicating that the analysis is performed in morphologically similar areas.

structure and rectangular shape of the specimens compared to the original sharp structure and shape of the printed specimens.

The sample that was not cross-linked started to lose its shape within 1 h, and after 24 h, the grid was basically transformed into jelly and the dimensional changes were not measurable. The grid that was cross-linked for 3 min after printing remained relatively solid in the PBS, even after 24 h. Slight swelling was noted, but due to the grid structure, no significant changes were observed on the outer edges, and the length of the outer edges varied from 36 to 37 mm after 24 h. Swelling seemed to happen mainly toward the empty holes inside the grid. Based on this observation, it was determined that the print pattern can have a significant effect on the dimensional stability of the 3D-printed structures in variable conditions.

**3.6. Conditioning Testing.** Water uptake is a relevant characteristic for materials intended for applications such as wound dressing. Water-vapor-uptake values of the printed ATG50 specimens as a function of conditioning time at 95% relative humidity are presented in Figure 8. The structures made of the pure TCNF hydrogel absorbed moisture significantly slower compared to the ones made of the TCNF–alginate–glycerin mixtures. The nonfreeze-dried TCNF–alginate–glycerin specimens showed quite similar moisture uptake regardless of whether they were cross-linked or not. The cross-linked specimens retained their shape; however, the excess water (or other substances) started to leak out of the specimens toward the end of the test.

Volumetric swelling of the printed ATG50 structures differed considerably from that of the TCNF (Figure 8b). The ATG50 structures without cross-linking gradually swell until they completely lose their shape after a few days of conditioning at 95% RH. Cross-linking decreases the dimensional changes of the ATG50 structures, and as mentioned above, the original shape of the structure is still recognizable after 4 days of exposure to high humidity. Contrary to the other printed structures, the TCNF specimens shrink, and the shape of the structure slightly changes.

**3.7. Compression Measurements.** To study the compressibility of the hydrogels, their mechanical characteristics were evaluated. The compressive strain values, shown in Figure 8c, indicate clearly that post-treatment has an effect on compressibility. The freeze-dried TCNF and ATG50 samples were softer and spongier. Especially the TCNF sample was foamy after freeze-drying (as shown in Figure 1d) and thus compressed easily. The compressive force needed for a 30% compressive strain was around 5 N, while the other samples needed approximately 10 N or more. This was clearly connected to high moisture uptake and dimensional changes with the freeze-dried ATG50. Otherwise, the compressive force correlated with density and no clear relation to the amount of glycerin was noticed. The cross-linked sample ATG50 + CaCl<sub>2</sub> had a slightly lower compression force at 30% strain but lower density. The cross-linking created a dense film around the sample, and thus, drying was restricted. The cross-linked sample ATG50 + CaCl<sub>2</sub> had a more rubber-like surface compared to the ATG50.

**3.8. Covalent Conjugation of Avidin to TCNF.** To enable the biofunctionalization of the printing material with different types of biotinylated molecules, charge-neutralized chimeric avidin was covalently conjugated to TCNF using NHS and EDC chemistry (Figure 9a). We first evaluated if the protein–nanocellulose complex could be harvested from the solution by using a 0.2  $\mu$ m filter. A filtered conjugated sample

(S) and a control (C) sample without chemical coupling were analyzed by measuring the electrophoretic mobility using SDS-PAGE (Figure 9b). We observed no protein band in the samples, which indicates that the nChiAvid protein associates with the nanocellulose and becomes trapped into the filter.

The chemical nature of the interaction between nChiAvid and TCNF was therefore evaluated by treating the conjugated samples with SDS detergent without filtering the samples. nChiAvid is a tetrameric protein containing several surface exposed amine groups and may form one or several covalent bonds with the carboxyl groups of TCNF. Once conjugated with nanocellulose, the large molecular size of the complex ( $\sim 200$ – $300$  kg/mol)<sup>29</sup> results in very low mobility in the gel electrophoresis. When heated to 50  $^{\circ}$ C, nChiAvid remains a tetramer in both the absence and the presence of biotin (Figure 9b). For the samples conjugated covalently with nanocellulose, no protein band is observed on the gel after heating to 50  $^{\circ}$ C, indicating covalent bonding between nChiAvid and TCNF. In contrast, a band corresponding to tetrameric nChiAvid is observed for the control samples without chemical coupling, indicating that nonspecifically bound nChiAvid is separated from TCNF by heat treatment and electrophoretic separation.

When heated to 100  $^{\circ}$ C, nChiAvid dissociates into monomers in the absence of biotin, but the presence of biotin partially stabilizes the protein, and both monomers and tetramers are detected (Figure 9b). For the covalently conjugated sample in the absence of biotin, some monomers can be detected after boiling, but there is a significant decrease as compared to the control sample without chemical coupling. This suggests that some of the avidins are conjugated covalently via one to three subunits of the tetramer, and boiling can release the nonconjugated monomers. The presence of biotin stabilizes nChiAvid, and no protein is detected for the covalently conjugated sample, which further supports the model.

Overall, this experiment indicates that the covalent conjugation between nChiAvid and TCNF has been successful. However, not all of the avidin monomers are covalently bound to nanocellulose, and the nonconjugated subunits can be released by boiling the sample in the presence of SDS detergent. Because nChiAvid is a stable tetramer in physiological conditions, the resulting composite can be utilized for further functionalization via avidin–biotin interaction.

**3.9. Functionalization of Printed Samples by Biotin Conjugates.** To demonstrate the presence and activity of avidin within the hydrogel after 3D printing, the printed samples were incubated with the fluorescent biotin derivative DY634-biotin and with the biotin–EGFP fusion protein. The samples were imaged by confocal microscope to determine the fluorescence within the samples. In addition, bright-field images were captured to indicate similar morphology of all fluorescently stained samples. The 3D-printed samples showed clearly fluorescent areas inside the hydrogel when labeled with DY634-biotin (results not shown) and biotin–EGFP (Figure 9c). The fluorescent intensity within sample increased at increasing concentration of biotin–EGFP, as expected. Samples that were incubated with free D-biotin before the addition of fluorescent biotin–conjugates showed no fluorescence, which indicates that D-biotin had blocked the binding sites of avidin, and the biotinylated fluorescent conjugates were bound within the hydrogel through a specific avidin–biotin interaction as the nonbound labels were efficiently washed away. Because the DY634-biotin has a molecular weight of approximately 1330 Da, it indicates that the hydrogel can be functionalized



with small biotinylated molecules. Moreover, biotin–EGFP is an ~40 kDa protein, which indicates that the 3D-printed hydrogel could also be functionalized with other bioactive molecules, such as growth factors or antibodies.

#### 4. CONCLUSIONS

Several biobased hydrogel compositions were benchmarked to be used as a printing paste for 3D printing. A combination of alginate, cellulose nanofibrils, and glycerin enabled excellent printability and dimensional stability at room temperature. Collapsing of the printing paste can be avoided by increasing the share of nonvolatile components and by using an effective strength additive such as CNFs. In addition, the print pattern can have a significant effect on the shape fidelity and stability. According to the buffer tests, the 3D printing of porous structures reduced excess deformation of the objects, especially when the printed structure was cross-linked with  $\text{CaCl}_2$ . Voids within the structure provided room for swelling in moist and wet conditions. This can be a desired property in wound-healing applications, in which compressive forces may cause irritation and pain. Nevertheless, more work is needed to improve the structural stability of the printed material, especially in wet or moist conditions and in prolonged use. This could be achieved with other cross-linking methods or by using alternative polymeric reinforcing materials such as polyethylene glycol (PEG) or polypropylene glycol (PPG), which enable the formation of more-hydrophobic patterns when cured.

Our work also demonstrates the feasibility of CFD simulations for predicting dependencies between key process parameters, such as printer-head geometry, operating pressure, and printing speed, and relevant outcomes such as mass flux and shear-stress distribution within the printer head and the resolution of the printed line. The same models reveal the sensitivity of the printing outcome to the hydrogel rheology, which can be used for optimizing printing paste formulations.

The described avidin-functionalized nanocellulose–alginate material provides a generic platform for the immobilization of bioactive components via biotin–avidin interaction. This interaction has been used in numerous applications, and a vast number of biotinylated molecules are commercially available. The functionalization of 3D-printed samples was demonstrated by attaching a fluorescently labeled biotin or a biotinylated green fluorescent protein via covalently linked avidins. Therefore, the described material could most probably be tailored to meet the needs in cell-based applications that require specific adhesion mediating signals, such as Arg–Gly–Asp (RGD) peptide. It may also prove to be suitable for studies on the controlled release of therapeutic molecules such as growth factors or antimicrobial agents such as antibiotics. Ultimately, 3D printing could provide the means for creating customized implant and wound-healing products with internal gradients of therapeutic agents and their gradual release. In addition, we envision potential use for the material in the development of wearable biosensors.

#### ■ ASSOCIATED CONTENT

##### ■ Supporting Information

The Supporting Information is available free of charge on the ACS Publications website at DOI: 10.1021/acsami.7b02756.

Additional details on thixotropic behavior of the TCNF hydrogel, composition of the PBS buffer, and additional buffer tests. (PDF)

#### ■ AUTHOR INFORMATION

##### Corresponding Author

\*E-mail: [vesa.hytonen@uta.fi](mailto:vesa.hytonen@uta.fi). Phone: (+358)-40-190-1517.

##### ORCID

Antti Paajanen: 0000-0002-4250-6363

Vesa P. Hytönen: 0000-0002-9357-1480

##### Author Contributions

J.L., P.L., and A.P. contributed equally to this work. All authors have given their approval to the final version of the manuscript.

##### Notes

The authors declare no competing financial interest.

#### ■ ACKNOWLEDGMENTS

Funding from the Academy of Finland (grant no. 290506) and infrastructural support from Biocenter Finland are gratefully acknowledged. Asta Nurmela (VTT) is acknowledged for assistance with the 3D printing experiments. We thank Ulla Kiiskinen (U. Tampere) and Niklas Kähkönen (U. Tampere) for preparing the buffers, Ulla Salonen (VTT) and Hannes Orelma (VTT) for preparing and imaging the printing pastes, and Martina Lille (VTT) for assistance with the compression tests.

#### ■ REFERENCES

- (1) ISO/ASTM. SFS-EN ISO/ASTM 52900:2017. Additive Manufacturing—General Principles—Terminology; ISO: Helsinki, Finland, 2017.
- (2) Wohlers Associates Inc. *Wohlers Report 2016:3D Printing and Additive Manufacturing State of the Industry Annual Worldwide Progress Report*; Wohlers Associates Inc.: Fort Collins, Colorado, 2016.
- (3) Mironov, V.; Kasyanov, V.; Markwald, R. R. Organ Printing: from Bioprinter to Organ Biofabrication Line. *Curr. Opin. Biotechnol.* **2011**, *22* (5), 667–73.
- (4) Rengier, F.; Mehndiratta, A.; Von Tengg-Kobligk, H.; Zechmann, C. M.; Unterhinninghofen, R.; Kauczor, H. U.; Giesel, F. L. 3D Printing Based on Imaging Data: Review of Medical Applications. *Int. J. Comput. Assist. Radiol. Surg.* **2010**, *5*, 335–341.
- (5) Murphy, S. V.; Atala, A. 3D Bioprinting of Tissues and Organs. *Nat. Biotechnol.* **2014**, *32*, 773–785.
- (6) Markstedt, K.; Mantas, A.; Tournier, I.; Martínez, Á. H.; Hägg, D.; Gatenholm, P. 3D Bioprinting Human Chondrocytes with Nanocellulose-Alginate Bioink for Cartilage Tissue Engineering Applications. *Biomacromolecules* **2015**, *16* (5), 1489–1496.
- (7) Rees, A.; Powell, L. C.; Chinga-Carrasco, G.; Gethin, D. T.; Syverud, K.; Hill, K. E.; Thomas, D. W. 3D Bioprinting of Carboxymethylated-Periodate Oxidized Nanocellulose Constructs for Wound Dressing Applications. *BioMed Res. Int.* **2015**, *2015*, 7.
- (8) Rutz, A. L.; Hyland, K. E.; Jakus, A. E.; Burghardt, W. R.; Shah, R. N. A Multimaterial Bioink Method for 3D Printing Tunable, Cell-Compatible Hydrogels. *Adv. Mater.* **2015**, *27*, 1607–1614.
- (9) Müller, M.; Öztürk, E.; Arlov, Ø.; Gatenholm, P.; Zenobi-Wong, M. Alginate Sulfate-Nanocellulose Bioinks for Cartilage Bioprinting Applications. *Ann. Biomed. Eng.* **2017**, *45*, 210–223.
- (10) Ma, X.; Li, R.; Zhao, X.; Ji, Q.; Xing, Y.; Sunarso, J.; Xia, Y. Biopolymer Composite Fibres Composed of Calcium Alginate Reinforced with Nanocrystalline Cellulose. *Composites, Part A* **2017**, *96*, 155–163.
- (11) Siqueira, G.; Kokkinis, D.; Libanori, R.; Hausmann, M. K.; Gladman, A. S.; Neels, A.; Tingaut, P.; Zimmermann, T.; Lewis, J. A.; Studart, A. R. Cellulose Nanocrystal Inks for 3D Printing of Textured Cellular Architectures. *Adv. Funct. Mater.* **2017**, *27*, 1604619–1–10.

- (12) Axpe, E.; Oyen, M. L. Applications of Alginate-Based Bioinks in 3D Bioprinting. *Int. J. Mol. Sci.* **2016**, *17* (12), 1976–1–11.
- (13) Hölzl, K.; Lin, S.; Tytgat, L.; Van Vlierberghe, S.; Gu, L.; Ovsianikov, A. Bioink Properties Before, During and After 3D Bioprinting. *Biofabrication* **2016**, *8* (3), 032002–1–19.
- (14) Peppas, N. A.; Khare, A. R. Preparation, Structure and Diffusional Behavior of Hydrogels in Controlled Release. *Adv. Drug Delivery Rev.* **1993**, *11* (1–2), 1–35.
- (15) Ullah, F.; Othman, M. B. H.; Javed, F.; Ahmad, Z.; Akil, H. M. Classification, Processing and Application of Hydrogels: A Review. *Mater. Sci. Eng., C* **2015**, *57*, 414–433.
- (16) Buwalda, S. J.; Boere, K. W. M.; Dijkstra, P. J.; Feijen, J.; Vermonden, T.; Hennink, W. E. Hydrogels in a Historical Perspective: From Simple Networks to Smart Materials. *J. Controlled Release* **2014**, *190*, 254–273.
- (17) Gainza, G.; Villullas, S.; Pedraz, J. L.; Hernandez, R. M.; Igartua, M. Advances in Drug Delivery Systems (DDSs) to Release Growth Factors for Wound Healing and Skin Regeneration. *Nanomedicine* **2015**, *11* (6), 1551–1573.
- (18) Green, N. M. Avidin. 3. The Nature of the Biotin-binding Site. *Biochem. J.* **1963**, *89* (3), 599–609.
- (19) Vikholm-Lundin, I.; Auer, S.; Paakkunainen, M.; Määttä, J. A. E.; Munter, T.; Leppiniemi, J.; Hytönen, V. P.; Tappura, K. Cysteine-tagged Chimeric Avidin Forms High Binding Capacity Layers Directly on Gold. *Sens. Actuators, B* **2012**, *171–172*, 440–448.
- (20) Taskinen, B.; Zauner, D.; Lehtonen, S. I.; Koskinen, M.; Thomson, C.; Kähkönen, N.; Kukkurainen, S.; Määttä, J. A. E.; Ihalainen, T. O.; Kulomaa, M. S.; Gruber, H. J.; Hytönen, V. P. Switchavidin: Reversible Biotin-Avidin-Biotin Bridges with High Affinity and Specificity. *Bioconjugate Chem.* **2014**, *25* (12), 2233–2243.
- (21) Laitinen, O. H.; Hytönen, V. P.; Nordlund, H. R.; Kulomaa, M. S. Genetically Engineered Avidins and Streptavidins. *Cell. Mol. Life Sci.* **2006**, *63* (24), 2992–3017.
- (22) Saito, T.; Nishiyama, Y.; Putaux, J.-L.; Vignon, M.; Isogai, A. Homogeneous Suspensions of Individualized Microfibrils from TEMPO-Catalyzed Oxidation of Native Cellulose. *Biomacromolecules* **2006**, *7* (6), 1687–1691.
- (23) Ray, S.; Steven, R. T.; Green, F. M.; Höök, F.; Taskinen, B.; Hytönen, V. P.; Shard, A. G. Neutralized Chimeric Avidin Binding at a Reference Biosensor Surface. *Langmuir* **2015**, *31* (6), 1921–1930.
- (24) Hytönen, V. P.; Määttä, J. A. E.; Nyholm, T. K. M.; Livnah, O.; Eisenberg-Domovich, Y.; Hyre, D.; Nordlund, H. R.; Hörhä, J.; Niskanen, E. A.; Paldanius, T.; Kulomaa, T.; Porkka, E. J.; Stayton, P. S.; Laitinen, O. H.; Kulomaa, M. S. Design and Construction of Highly Stable, Protease-Resistant Chimeric Avidins. *J. Biol. Chem.* **2005**, *280* (11), 10228–10233.
- (25) Kangas, H.; Lahtinen, P.; Sneek, A.; Saariaho, A.-M.; Laitinen, O.; Hellén, E. Characterization of Fibrillated Celluloses. A Short Review and Evaluation of Characteristics with a Combination of Methods. *Nord. Pulp Pap. Res. J.* **2014**, *29* (1), 129–143.
- (26) Mewis, J.; Wagner, N. J. Thixotropy. *Adv. Colloid Interface Sci.* **2009**, *147–148*, 214–227.
- (27) Weller, H. G.; Tabor, G.; Jasak, H.; Fureby, C. A Tensorial Approach to Computational Continuum Mechanics Using Object-oriented Techniques. *Comput. Phys.* **1998**, *12* (6), 620–631.
- (28) Kumar, V.; Elfving, A.; Koivula, H.; Bousfield, D.; Toivakka, M. Roll-to-Roll Processed Cellulose Nanofiber Coatings. *Ind. Eng. Chem. Res.* **2016**, *55*, 3603–3613.
- (29) Hiraoki, R.; Ono, Y.; Saito, T.; Isogai, A. Molecular Mass and Molecular-Mass Distribution of TEMPO-Oxidized Celluloses and TEMPO-Oxidized Cellulose Nanofibrils. *Biomacromolecules* **2015**, *16* (2), 675–681.